

# Ultrafast electrical control of dipolaritonic circuits with a few femto-joul per bit power consumption

Dror Liran and Ronen Rapaport\*

Racah Institute of Physics, The Hebrew University of Jerusalem, Jerusalem 9190401, Israel

Kirk Baldwin and Loren Pfeiffer

Department of Electrical Engineering, Princeton University, Princeton, NJ, 08544 USA

Hui Deng

University of Michigan, Ann Arbor, MI 48109, USA

(Dated:)

The next generation of photonic circuits will require on-chip, ultrafast, compact, and energy-efficient components in a scalable platform to power technologies like quantum and neuromorphic computing. Here we present a significant advancement in ultrafast electrical control of highly non-linear hybrid light-matter quasi-particles, called waveguide exciton-dipolaritons, with extremely low power consumption. Our device, that was shown to perform as an optical transistor with an optical switching power as low as  $\sim 1$  fJ/operation, achieves a GHz-rate electrical modulation with a record-low total energy consumption  $\sim 3$  fJ/bit and a compact active area of down to  $25 \mu\text{m}^2$ . This work establishes waveguide-dipolariton platforms for scalable, electrically reconfigurable, ultra-low power photonic circuits for both classical and quantum computing and communication.

**Keywords:** dipolar exciton polaritons, photonic computing, optical modulators, optical transistor, neuromorphic computing, quantum photonics

**Introduction:** Integrated photonic circuits are most likely the best platform for the rapidly developed fields of optical information processing [1–5], including classical and quantum simulators and computers [6, 7], as well as neuromorphic calculators [8, 9]. The most crucial requirements for complex optically-based reconfigurable circuitry for neuromorphic and quantum calculations [8, 10], is the ability for a scalable, ultrafast *electrical* control of individual nodes with an ultra-low power consumption per node per operation, together with a strong nonlinear optical response.

Exciton polaritons (EP) [11], resulting from the strong coupling of confined photons and excitons in semiconductor heterostructures, are excellent building blocks for photonic circuits. They can be directly addressed and optically manipulated due to their photonic part, and have significant optical nonlinearities due to the matter-like, excitonic part. Recent demonstrations of ultrafast all-optical control of EP in microcavities, including optical switching [12–19], EP condensate-based photonic lattice simulators [6, 7, 20], and EP based neuromorphic computing [9, 21] are just a few examples of the promise of EP platforms.

For a truly complex photonic circuitry, electrically controlled EP-based nonlinear nodes should be densely integrated into monolithic chip geometries. For microcavity-based EP elements, only optical control has been demonstrated so far, which is inherently limited by scalability and optical loss [22]. Furthermore, significant optical power is required per node, typically

more extensive than  $10^3 \text{ J}/\text{node}/\text{operation}$  at 1GHz [12], and densely scaling up layers of nodes for deep circuits is a major challenge as microcavities cannot be easily stacked.

A more natural geometry for EP-based circuits is that of EP in chip-integrated waveguides, known as waveguide exciton-polaritons (WEP)[23, 24], for which various linear and non-linear photonic elements have been demonstrated recently in low loss devices [25–30]. These recent demonstrations set WEP as a promising on-chip platform for complex photonic circuitry.

An important step towards locally reconfigurable and scalable WEP circuits is the recent realization of electrically controlled elements based on *electrically gated dipolar WEP (DWEP)*. In such devices, wide quantum wells (QW) are embedded inside an optical waveguide. With top electrical gates at desired locations, tunable electric fields can be applied perpendicular to the QW plane and to the WEP propagation direction. These fields induce a quantum confined Stark effect on the WEP through their excitonic component, leading to an energy shift of the whole DWEP dispersion under the gate [24], allowing electrical control of the DWEP propagation. Furthermore, the local electric field polarizes the DWEP, resulting in WEP having an induced electric dipole. These DWEP then interact very strongly with each other, leading to a polariton record-high effective nonlinearity that is up to two-orders of magnitude enhanced as compared to unpolarized EP [28]. This huge enhancement is explained via a combination of direct

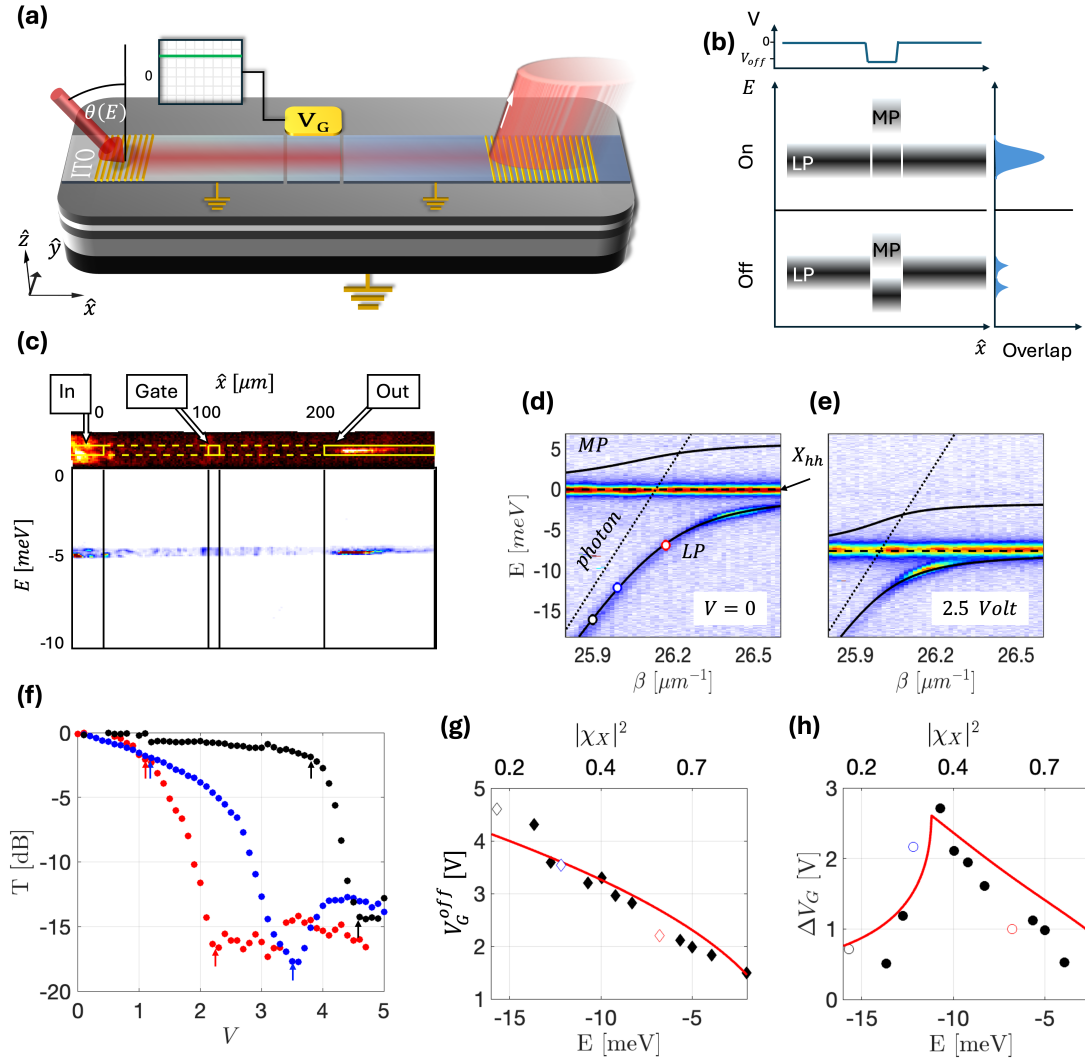


**Figure 1. Setup and electric field dependence of experiments with gated-DWEP devices:** (a) Schematic diagram of the device structure, with the ITO electrode divided into three parts: the gate  $V_G$  and the unbiased channel. The incident laser excites the sample at  $\theta(E)$  to satisfy the WEP dispersion. The transmitted light is a function of the field amplitude  $V_G$ . (b) Energy diagram for the polariton switching. Top Panel: schematic of the voltage values along the waveguide. Middle panel: "on" - the gate is flat with the channel allowing the polaritons to transmit. Bottom panel: "off" - the gate is biased such that the states from the channel meet the LP-MP gap in the gate, and the polaritons do not transmit. (c) Top panel: a real-space image of the WEP experiment. The laser is injected in the left grating, and the WEP signal couples out from the right grating. Bottom panel: a spectrally resolved imaging measurement of the WEP. (d) and (e) measured WEP Dispersion at  $V_G = 0$  and  $V_G = 2.5$  V/ $\mu\text{m}$ , respectively. The plots show the energy  $E$  as a function of the wavevector ( $\beta$ ). The lower polariton (LP) and middle polariton (MP) model fits are indicated by solid black lines. A flat dashed line marks the heavy-hole exciton, and a dotted diagonal line marks the bare WG-photon. The colored dots in (d) correspond to the three curves in (f). (f) The transmission in the channel as a function of  $V_G$  for three different WEP excitation energies  $E = -7, -12, -16$  meV marked in (d) respectively. The arrows mark the points defined as the on-off transition. (g) The voltage value ( $V_G$ ) of the first minimum in the transmission. The values for the curves in (f) appear in the corresponding color. The red line plots the voltage value required for the exciton to shift such energy. (h) The voltage difference ( $\Delta V_G$ ) between the first minimum in transmission and a transmission of 0.6. The two colored points represent the corresponding transitions marked in figure (f) by colored arrows. The red lines mark the model prediction.

dipole-dipole interactions and dipolar screening of the applied field [29], together with the reduction of correlations due to the ultralight mass of the DWEP [31]. The unique properties of such DWEP were utilized to demonstrate an electrically controlled photon switch, as is illustrated in Fig. 1, and a strongly nonlinear optical transistor, both operating with only few hundred photons, very low switching voltages of  $\sim 1\text{V}$ , and small footprints of  $\sim 100\text{ }\mu\text{m}^2$  [29]. Recently, electrically tunable quantum correlations and a partial 2-photon blockade was demonstrated, showing potential for realizing DWEP for electrically switchable, universal 2-photon gates [32]. If such photonic-building blocks can be reconfigured and operated at ultrafast rates, and can be shown to be scalable in terms of electrical power consumption and size, they will open up a route towards universal photonic computation on-chip.

In this work, we demonstrate a fast, sub-nanosecond temporal control of such nonlinear DWEP-switches operating at record-low powers of sub 3 Femto-Joule/bit and a very small footprint of  $< 50\mu\text{m}^2$  per node, a significant step towards complex optical circuitry based on WEP.

**DWEP device characterization:** the device used in these experiments (Fig. 1(a)) is  $200\text{ }\mu\text{m}$  long and  $5\text{ }\mu\text{m}$  wide waveguide channel, optically defined by an indium tin oxide (ITO) strip, with two Au diffraction gratings for input and output at either end. The waveguide itself is constructed out of an  $Al_{0.4}Ga_{0.6}As$  core with 12 embedded 20nm-wide  $GaAs$  quantum wells (QWs). For details on the full sample fabrication, see Ref. [29]. The strong interaction of the transverse-electric (TE) polarized waveguide mode with the heavy-hole ( $hh$ ) and light-hole ( $lh$ ) excitons leads to the formation of three polariton modes: Lower-Polariton (LP), Middle-Polariton (MP), and Upper-polariton (UP) [24]. Each polariton mode is a superposition of the bare TE-photon and the two excitons, represented as  $|\psi_{pol}(\beta)\rangle^i = \chi_{ph}^i(\beta)|\psi_{ph}\rangle + \chi_{hh}^i(\beta)|\psi_{hh}\rangle + \chi_{lh}^i(\beta)|\psi_{lh}\rangle$ , where  $i = LP, MP$ , and  $UP$  respectively, and the Hopfield coefficients satisfy  $|\chi_{hh}|^2 + |\chi_{lh}|^2 + |\chi_{ph}|^2 = 1$ . The total exciton fraction of the polariton is defined here as  $|\chi_X(\beta)|^2 = 1 - |\chi_{ph}(\beta)|^2$ . LP-polaritons having  $|\psi_{pol}(\beta)\rangle^{LP}$ ,  $E_{LP}(\beta)$  can be excited at the left grating by a resonant laser (Ti:Sa, CW) with its energy and incidence angle matching the desired position on the polariton dispersion. We define a relative DWEP dispersion  $E(\beta) = E_{LP}(\beta) - E_{hh}$ , measured with respect to the unbiased  $hh$ -exciton energy,  $E_{hh}$ . Such dispersions are shown in Fig. 1(a, d). The output signal is collected from the right grating and imaged onto a spectrometer. Cross-polarization is employed in both the excitation and emission paths to isolate the

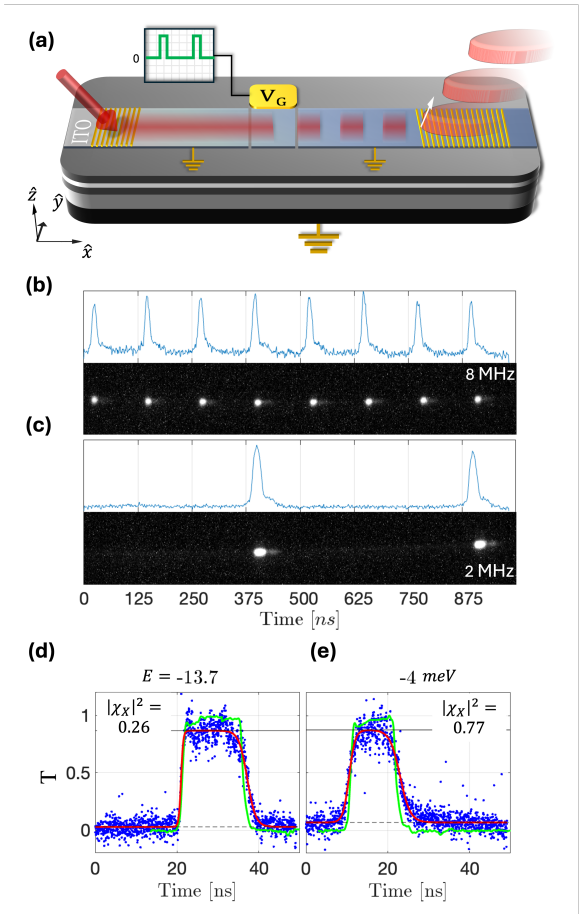


**Figure 2. Pulse Modulation:** (a) Illustration of the device response to a square voltage modulation of the gate. (b) and (c) Time-resolved measurement of the transmitted signal at 8 and 2 MHz, respectively. The bottom panel plots the raw data from the streak camera, while the top panel plots the integrated amplitude. (d) and (e) Normalized time-domain pulse transmission (blue dots) for two different polariton energies  $E = -13.7\text{ meV}$  and  $E = -4\text{ meV}$ , plotted along the normalized electric signal input. The data is fitted to a pulse function (red line). The black lines mark the "on" (solid) and "off" (dashed) states.

polariton emission from the scattered laser light. Additionally, spatial filtering further reduces laser scattering (see Fig. S2 in the SM). To allow independent control of the electric field in each section, the ITO strip that defines the optical waveguide [29] is divided into three sections by a  $< 1\mu\text{m}$  gap in the electrode. The middle section, named the "gate", is electrically biased. The gate is  $10\mu\text{m}$  long and is centered between the input and output gratings. The outer sections (hereafter the "channel") are held at zero bias.

When a field is applied to the gate, the DWEP transmission between the input and output gratings de-

creases due to the reduced overlap of the DWEP density of states under the gate and in the channel [29]; an illustration of the mechanism is presented in Fig. 1(b), where minimum transmission occurs when the gate voltage  $V_G$  is shifting the LP energy by exactly one Rabi frequency  $\Omega(V_G)$ , i.e.,  $\Delta E(\Delta V_G) = \Omega(V_G)$ , where  $(\Delta V_G)$  is the voltage difference for switching between on and off states. Fig. 1(f) plots the DWEP transmission  $T$  (normalized to its maximum) as a function of the gate voltage ( $V_G$ ) for three different excitation energies  $E = -7, -12, -16\text{ meV}$ . Arrows on each curve indicate the  $T = 0.6$  (-2.2 dB) and minimal transmission points.

Such transmission curves are then used to extract  $V_G(E)$  required for blocking the DWEP propagation for different excitation energies, as plotted in Fig. 1(g). From the same transmission curves we also extract  $\Delta V_G(E)$ , Fig. 1(h). Interestingly,  $\Delta V_G(E)$  shows a non-monotonic behavior. This behavior arises from the non-linear dispersion of the DWEP,  $E(\beta)$ . For simplicity, we employ a two-mode WEP model, which allows us to derive the following expression:

$$\Delta V_G = V_G^{off} \left( 1 - \sqrt{\frac{-(E(\beta)_0 + \Omega(V_G))}{-E(\beta)_0}} \right) \quad (1)$$

Where  $E(\beta)_0 \equiv E(\beta, V_G = 0)$  is the polariton energy which the laser resonantly injects into the sample,  $V_G^{off} = \sqrt{\frac{-E(\beta)_0}{\alpha'}}$  is the voltage required to bring the exciton to the injection energy, and  $\alpha' = 1.53\text{ meV}/V^2$  [29] is the electric polarizability of the QW hh-exciton. The model, presented in detail in the SM, agrees well with the data, as is shown by the red lines in Fig. 1(g,h).

**Electrical modulation of DWEP:** to test the frequency response of the system, we injected WEP resonantly through the input grating using a CW laser, while modulating the gate voltage using a square electrical pulse  $f(t)$  with a nanosecond rise and fall times. The experiment was repeated with different periods and duty cycles, as depicted schematically in Fig. 2(a). The field amplitudes and offsets of the electrical modulation were selected based on the DC measurements presented in Fig. 1 (f-h), and can be represented by  $V(t) = V_G^{off} + \Delta V_G \times f(t)$ . The output signal was imaged onto a streak camera. Such Streak images for two different modulation frequencies are presented in Fig. 2(b,c). Fig. 2(d,e) presents the time-domain DWEP transmission of single pulses (blue dots) plotted on top of the modulating electric field (solid green line) for WEPs excited at  $-13.7, -4\text{ meV}$ , corresponding to excitonic fractions of  $|\chi_X|^2 = 0.26, 0.77$  respectively. The black lines indicate the “on” (solid) and “off” (dashed) states. The transmission data is fitted with a pulse

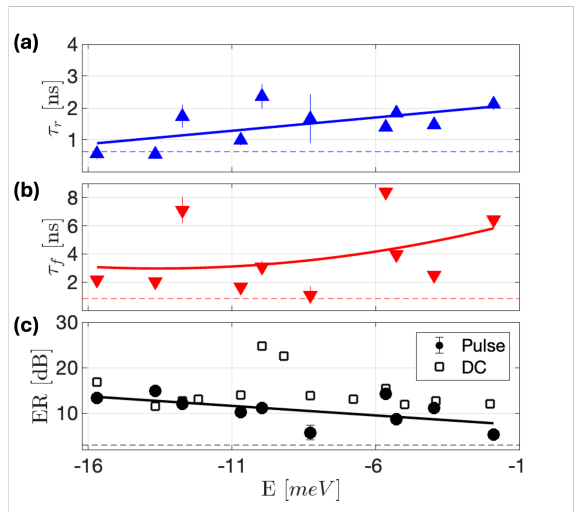


**Figure 3. Bandwidth, Extinction, and Power consumption:** (a) and (b) Extracted transition times (rise and fall) as a function of the excited WEP energy. The lines are guides to the eye. The error bars represent the fit uncertainty values. The dashed line marks the input voltage transition time. (c) Extinction ratios as a function of excited WEP energy. The line is a guide to the eye. A dashed black line marks the minimal required ER (3 dB). The corresponding DC extinction ratio is also plotted with empty squares.

function (red line):

$$T(t) = T_{on}/2 \times \left( \tanh\left(\frac{t - t_r}{\tau_r}\right) - \tanh\left(\frac{t - t_f}{\tau_f}\right) \right) + T_{off} \quad (2)$$

where  $\tau_r, \tau_f$  are the rise and fall times, respectively.

**Bandwidth:** From such fitting as above, we extracted  $\tau_r, \tau_f$ , as well as the extinction ratio (ER),  $ER = T_{on}/T_{off}$ , for various excitation energies, for electrical pulses with a 4MHz carrier frequency, and pulse durations of 15–20 ns. The extracted rise and fall times are plotted in Fig. 3(a,b), and are both smaller for lower energy DWEPs, corresponding to more photon-like polaritons. Rise times as short as 0.5ns and fall times as short as 1 ns are measured. As seen from Fig. 3(d,e), the optical signal of photon-like DWEPs follows the electrical pulse. This means that the electrical pulse generator still limits the rise and fall times and not intrinsically by the WEP system. Therefore, we conclude that our devices can operate at >GHz bandwidth.

**Extinction ratio:** the extinction ratio is shown for various DWEP energies in Fig. 3(c,d). Again, more photon-like DWEPs tend to have a higher extinction ratio, indicating more efficient switching. Importantly, these photon-dominated states also have faster propagation in the WG, lower propagation loss, and better

**Table I: Integrated electro-optic modulators**

Mechanism	Material	Power consumption [fJ/bit] @ 1 GHz <sup>a</sup>	ER [dB]	Footprint [μm <sup>2</sup> ]
DWEP (this work)	GaAs	~ 3 <sup>b</sup>	25 <sup>c</sup>	25 <sup>d</sup>
Pockels effect (MZI <sup>e</sup> ) [33]	LN	26	30	10 <sup>4</sup>
Carrier injection [34] <sup>f</sup>	Si	500	8	10 <sup>3</sup>
Plasmonic–organic–hybrid (MZI) [35]	Si and Au	2750	25 <sup>g</sup>	~ 10
MC EP (all optical) [12]	GaAs <sup>h</sup>	1980	12	1.6 × 10 <sup>3</sup>

<sup>a</sup> The power consumption was rescaled to a bit rate of 1GHz with duty-cycle of 0.5

<sup>b</sup> see the SM for a full derivation

<sup>c</sup> See DC measurements of ER in Fig. 3, limited by the SNR

<sup>d</sup> projected

<sup>e</sup> Mach-Zender Interometer

<sup>f</sup> The device with the lowest power consumption

<sup>g</sup> loss of 5dB per element

<sup>h</sup> Can also be realized in many other material systems, see Ref. [14]

in- and outcoupling efficiencies. *ER* values as high as 15dB are measured, limited only by the SNR of the Streak camera. To demonstrate that the actual *ER* values are higher, we plot the *ER* for the DC case, which had a better SNR of up to 25 dB.

**Energy consumption:** the energy consumption for our device is composed of two factors, the energy of photons in a cycle and the electrical energy to operate the switching, given by the current-voltage product in a cycle. To estimate this, we measured the current of the device during operation, with  $V_G^{off} = 3.1V$  and  $\Delta V_G$  of 2.25, we measured currents of  $I = 0.46$  and  $0.85 \mu A$ , respectively. For a duty cycle of  $R = 50\%$  and frequency of  $f = 1$  GHz, the energy consumption per operation is  $1.3fJ/bit$ ; the measurement details appear in the SM. Optically, the optical power required for the nonlinear DWEP-transistor operation is 1.2 fJ per cycle at 1 GHz is required; (see SM). Finally, electrical and optical energy consumption adds up to about  $2.5fJ$  per cycle at 1 GHz for a fully functional electrically-modulated transistor device.

**Discussion:** We demonstrated DWEP signal modulation with a bandwidth exceeding 1 GHz, primarily constrained by the limitations of the electrical pulse generator and the electronic circuitry, together with a very high extinction ratio. A proper electrical design can significantly improve the bandwidth, as was demonstrated in GaAs-based electro-optical devices that have achieved modulation frequencies up to 100GHz [36]. With a minimal footprint (down to  $25 \mu m^2$ ), such elements are well suited for high-density photonic circuitry. The footprint could be further reduced by shortening the gate length to a few times the WEP wavelength in the medium ( $\lambda \simeq 240nm$ ), and decreasing the channel width to  $\sim 0.5\mu m$  by side etching [25, 27], resulting in an overall footprint as small as  $\sim 1\mu m^2$  per node.

Remarkably, our device demonstrates overall power consumption smaller than  $3fJ/bit$ , which, as far as we

know, sets a record compared to other platforms, as detailed in the table. We emphasize that low power consumption per node per operation is a crucial factor in large-scale fast circuitry, including those designed for classical neuromorphic computing as well as for quantum computing. Both cases require a large amount of reconfigurable elements [37]. A further reduction in power consumption can be achieved by minimizing tunneling between the top and bottom contacts, as well as reducing the surface area of the electrical contacts, which in our current design constitute the most significant contributors to leakage currents.

Finally, the same device displays an electrically tunable, optical nonlinearity which is, as far as we know, the highest of any exciton-polariton-based system, and is comparable to that of Rydberg atoms [32]. As mentioned before, this led to a demonstration of a fully operational optical transistor operating with 1.2 fJ/bit [29], and to quantum correlations at the two-photon level [32], which can be controlled very accurately by the applied electric field. The current demonstration of local >GHz modulation of an optical node, will allow a reconfigurable polariton-based optical circuitry, where the linear and nonlinear function at each node can be controlled separately and be reconfigured each operation, making electrically polarized DWEP as excellent candidates for reconfigurable deep optical circuits for either neuromorphic or quantum processors in a monolithic platform. Low propagation loss is also essential for a deep photonic circuit, particularly at the quantum limit where signal amplification is impossible. Our current device has a propagation loss of approximately 4-10 dB/cm[25], with a lower loss for high photonic fractions, which is a typical value for photonic losses in AlGaAs WG systems. The photonic loss can be significantly reduced to 0.4 dB/cm by integrating AlGaAs on an insulator (AlGaAsOI) [38]. Given the achievable element density of AlGaAsOI, the effective loss

per number of elements compares with state-of-the-art silicon-on-insulator (SOI) systems. Finally, for full integration, the chip should also incorporate single-photon detectors, which have already been realized in similar AlGaAs systems using superconductor-nanowire single-photon detectors (SNSPDs) [5, 39].

## ACKNOWLEDGEMENTS

R.R. and D.L. acknowledge the support from the Israeli Science Foundation Grant 1087/22, and from the NSF-BSF Grant 2019737. H.D. acknowledges the support of the National Science Foundation under grant DMR 2004287, the Army Research Office under grant W911NF-17-1-0312, and the Air Force Office of Scientific Research under grant FA2386-21-1-4066, and the Gordon and Betty Moore Foundation under grant N031710. This research is funded in part by the Gordon and Betty Moore Foundation’s EPiQS Initiative, Grant GBMF9615 to L. N. Pfeiffer, and by the National Science Foundation MRSEC grant DMR 2011750 to Princeton University

---

\* Correspondence email address: ronenr@phys.huji.ac.il

- [1] Terry Rudolph. Why i am optimistic about the silicon-photonic route to quantum computing. *APL Photonics*, 2(3), 3 2017.
- [2] Wim Bogaerts, Daniel Pérez, José Capmany, David A.B. Miller, Joyce Poon, Dirk Englund, Francesco Morichetti, and Andrea Melloni. Programmable photonic circuits. *Nature* 2020 586:7828, 586(7828):207–216, 10 2020.
- [3] Peter L. McMahon. The physics of optical computing. *Nature Reviews Physics* 2023 5:12, 5(12):717–734, 10 2023.
- [4] Ali W. Elshaari, Wolfram Pernice, Kartik Srinivasan, Oliver Benson, and Val Zwiller. Hybrid integrated quantum photonic circuits. *Nature Photonics* 2020 14:5, 14(5):285–298, 4 2020.
- [5] Christof P. Dietrich, Andrea Fiore, Mark G. Thompson, Martin Kamp, and Sven Höfling. GaAs integrated quantum photonics: Towards compact and multi-functional quantum photonic integrated circuits. *Laser & Photonics Reviews*, 10(6):870–894, 11 2016.
- [6] Natalia G. Berloff, Matteo Silva, Kirill Kalinin, Alexis Askitopoulos, Julian D. Töpfer, Pasquale Cilibrizzi, Wolfgang Langbein, and Pavlos G. Lagoudakis. Realizing the classical XY Hamiltonian in polariton simulators. *Nature Materials* 2017 16:11, 16(11):1120–1126, 9 2017.
- [7] Sergey Alyatkin, Carles Milián, Yaroslav V. Kartashov, Kirill A. Sitnik, Ivan Gnušov, Julian D. Töpfer, Helgi Sigurðsson, and Pavlos G. Lagoudakis. Antiferromagnetic Ising model in a triangular vortex lattice of quantum fluids of light. *Science advances*, 10(34):eadj1589, 8 2024.
- [8] Bhavin J. Shastri, Alexander N. Tait, T. Ferreira de Lima, Wolfram H.P. Pernice, Harish Bhaskaran, C. D. Wright, and Paul R. Prucnal. Photonics for artificial intelligence and neuromorphic computing. *Nature Photonics* 2021 15:2, 15(2):102–114, 1 2021.
- [9] Dario Ballarini, Antonio Gianfrate, Riccardo Panico, Andrzej Opala, Sanjib Ghosh, Lorenzo Dominici, Vincenzo Ardizzone, Milena De Giorgi, Giovanni Lerario, Giuseppe Gigli, Timothy C. H. Liew, Michał Matuszewski, and Daniele Sanvitto. Polaritonic Neuromorphic Computing Outperforms Linear Classifiers. *Nano Letters*, 20(5):3506–3512, 5 2020.
- [10] Sara Bartolucci, Patrick Birchall, Hector Bombín, Hugo Cable, Chris Dawson, Mercedes Gimeno-Segovia, Eric Johnston, Konrad Kieling, Naomi Nickerson, Mihir Pant, Fernando Pastawski, Terry Rudolph, and Chris Sparrow. Fusion-based quantum computation. *Nature Communications* 2023 14:1, 14(1):1–9, 2 2023.
- [11] Hui Deng, Hartmut Haug, and Yoshihisa Yamamoto. Exciton-polariton Bose-Einstein condensation. *Reviews of Modern Physics*, 82(2):1489–1537, 5 2010.
- [12] D. Ballarini, M. De Giorgi, E. Cancellieri, R. Houdre, E. Giacobino, R. Cingolani, A. Bramati, G. Gigli, and D. Sanvitto. All-optical polariton transistor. *Nature Communications*, 4:1778, 4 2013.
- [13] A. Amo, T. C.H. Liew, C. Adrados, R. Houdré, E. Giacobino, A. V. Kavokin, and A. Bramati. Exciton-polariton spin switches. *Nature Photonics*, 4(6):361–366, 6 2010.
- [14] Daniele Sanvitto and Stéphane Kéna-Cohen. The road towards polaritonic devices. *Nature Materials*, 15(10):1061–1073, 10 2016.
- [15] Félix Marsault, Hai Son Nguyen, Dimitrii Tanese, Aristide Lemaître, Elisabeth Galopin, Isabelle Sagnes, Alberto Amo, and Jacqueline Bloch. Realization of an all optical exciton-polariton router. *Applied Physics Letters*, 107(20):201115, 11 2015.
- [16] C. Sturm, D. Tanese, H.S. Nguyen, H. Flayac, E. Galopin, A. Lemaître, I. Sagnes, D. Solnyshkov, A. Amo, G. Malpuech, and J. Bloch. All-optical phase modulation in a cavity-polariton Mach-Zehnder interferometer. *Nature Communications*, 5(1):3278, 2 2014.
- [17] T. Gao, P. S. Eldridge, T. C. H. Liew, S. I. Tsintzos, G. Stavrinidis, G. Deligeorgis, Z. Hatzopoulos, and P. G. Savvidis. Polariton condensate transistor switch. *Physical Review B*, 85(23):235102, 6 2012.
- [18] Denis A. Sannikov, Anton V. Baranikov, Anton D. Putintsev, Mikhail Misko, Anton V. Zasedatelev, Ullrich Scherf, and Pavlos G. Lagoudakis. Room temperature, cascadable, all-optical polariton universal gates. *Nature Communications* 2024 15:1, 15(1):1–7, 6 2024.
- [19] Mikhail A. Masharin, Tatiana Oskolkova, Furkan Isik, Hilmi Volkan Demir, Anton K. Samusev, and Sergey V. Makarov. Giant Ultrafast All-Optical Modulation Based on Exceptional Points in Exciton-Polariton Per-

- ovskite Metasurfaces. *ACS Nano*, 18(4):3447–3455, 1 2024.
- [20] T. Jacqmin, I. Carusotto, I. Sagnes, M. Abbarchi, D. D. Solnyshkov, G. Malpuech, E. Galopin, A. Lemaître, J. Bloch, and A. Amo. Direct observation of Dirac cones and a flatband in a honeycomb lattice for polaritons. *Physical Review Letters*, 112(11):116402, 3 2014.
- [21] Andrzej Opala, Krzysztof Tyszka, Mateusz Kędziora, Magdalena Furman, Amir Rahmani, Stanisław Świerczewski, Marek Ekielski, Anna Szerling, Michał Matuszewski, and Barbara Piętka. Room temperature exciton-polariton neural network with perovskite crystal. *ArXiv 2412.10865*, 12 2024.
- [22] Anton V. Zasedatelev, Anton V. Baranikov, Darius Urbonas, Fabio Scafirimuto, Ullrich Scherf, Thilo Stöferle, Rainer F. Mahrt, and Pavlos G. Lagoudakis. A room-temperature organic polariton transistor. *Nature Photonics* 2019 13:6, 13(6):378–383, 3 2019.
- [23] P. M. Walker, L. Tinkler, M. Durska, D. M. Whittaker, I. J. Luxmoore, B. Royall, D. N. Krizhanovskii, M. S. Skolnick, I. Farrer, and D. A. Ritchie. Exciton polaritons in semiconductor waveguides. *Applied Physics Letters*, 102(1), 2013.
- [24] Itamar Rosenberg, Yotam Mazuz-Harpaz, Ronen Rapaport, Kenneth West, and Loren Pfeiffer. Electrically controlled mutual interactions of flying waveguide dipolaritons. *Physical Review B*, 93(19):195151, 5 2016.
- [25] Dror Liran, Itamar Rosenberg, Ken West, Loren Pfeiffer, and Ronen Rapaport. Fully Guided Electrically Controlled Exciton Polaritons. *ACS Photonics*, 5(11):4249–4252, 2018.
- [26] P. M. Walker, L. Tinkler, B. Royall, D. V. Skryabin, I. Farrer, D. A. Ritchie, M. S. Skolnick, and D. N. Krizhanovskii. Dark Solitons in High Velocity Waveguide Polariton Fluids. *Physical Review Letters*, 119(9):097403, 8 2017.
- [27] D.G. Suarez-Forero, Riminiucci F., Ardizzone V., Karpowicz N., Maggiolini E., Macorini G., Lerario G., Todisco F., De Giorgi M., Dominici L., Ballarini D., Gigli G., Lanotte A.S., West K., Baldwin K., Pfeiffer L., and Sanvitto D. Enhancement of Parametric Effects in Polariton Waveguides Induced by Dipolar Interactions. *Physical Review Letters*, 126(13):137401, 3 2021.
- [28] Itamar Rosenberg, Dror Liran, Yotam Mazuz-Harpaz, Kenneth West, Loren Pfeiffer, and Ronen Rapaport. Strongly interacting dipolar-polaritons. *Science Advances*, 4(10):eaat8880, 10 2018.
- [29] Dror Liran, Ronen Rapaport, Jiaqi Hu, Nathaniel Lydick, Hui Deng, and Loren Pfeiffer. Electrically Controlled Photonic Circuits of Field-Induced Dipolaritons with Huge Nonlinearities. *Physical Review X*, 14(3):031022, 8 2024.
- [30] Davide Nigro, Vincenzo D’Ambrosio, Daniele Sanvitto, and Dario Gerace. Integrated quantum polariton interferometry. *Communications Physics* 2022 5:1, 5(1):1–10, 2 2022.
- [31] E. R. Christensen, A. Camacho-Guardian, O. Cotlet, A. Imamoglu, M. Wouters, G. M. Bruun, and I. Carusotto. Microscopic theory of polariton-polariton interactions. *Physical Review B*, 110(19):195435, 11 2024.
- [32] Yoad Ordan, Dror Liran, Kirk W. Baldwin, Loren Pfeiffer, Hui Deng, and Ronen Rapaport. Electrically tunable quantum correlations of dipolar polaritons with micrometer-scale blockade radii. *ArXiv 2411.12059*, 11 2024.
- [33] Cheng Wang, Mian Zhang, Xi Chen, Maxime Bertrand, Amirhassan Shams-Ansari, Sethumadhavan Chandrasekhar, Peter Winzer, and Marko Lončar. Integrated lithium niobate electro-optic modulators operating at CMOS-compatible voltages. *Nature*, 562(7725):101–104, 10 2018.
- [34] G. T. Reed, G. Mashanovich, F. Y. Gardes, and D. J. Thomson. Silicon optical modulators. *Nature Photonics*, 4(8):518–526, 8 2010.
- [35] Christian Haffner, Wolfgang Heni, Yuriy Fedoryshyn, Arne Josten, Benedikt Baeuerle, Claudia Hoessbacher, Yannick Salamin, Ueli Koch, Nikola Dordevic, Pol Mousel, Romain Bonjour, Alexandros Emboras, David Hillerkuss, Pascal Leuchtmann, Delwin L. Elder, Larry R. Dalton, Christian Hafner, and Juerg Leuthold. Plasmonic Organic Hybrid Modulators—Scaling Highest Speed Photonics to the Microscale. *Proceedings of the IEEE*, 104(12):2362–2379, 12 2016.
- [36] CY Chang and F Kai. *GaAs high-speed devices: physics, technology, and circuit applications*. Wiley, 1st edition edition, 1994.
- [37] M. de Cea, A. H. Atabaki, and R. J. Ram. Energy harvesting optical modulators with sub-attojoule per bit electrical energy consumption. *Nature Communications*, 12(1):2326, 4 2021.
- [38] Lin Chang, Weiqiang Xie, Haowen Shu, Qi Fan Yang, Boqiang Shen, Andreas Boes, Jon D. Peters, Warren Jin, Chao Xiang, Songtao Liu, Gregory Moille, Su Peng Yu, Xingjun Wang, Kartik Srinivasan, Scott B. Papp, Kerry Vahala, and John E. Bowers. Ultra-efficient frequency comb generation in AlGaAs-on-insulator microresonators. *Nature Communications* 2020 11:1, 11(1):1–8, 3 2020.
- [39] Giulia Digeronimo, Maurangelo Petruzzella, Simone Birindelli, Rosalinda Gaudio, Sartoon Fattah Poor, Frank Van Otten, and Andrea Fiore. Integration of Single-Photon Sources and Detectors on GaAs. *Photonics*, 3(4):55, 10 2016.

## Supplementary Information

The Supplementary Information contains supporting calculations, a description of the optical setup, and raw data Images for DC and pulsed experiments.

### VOLTAGE MODULATION FOR DWEP SWITCHING - MODEL

Here we develop a simple model for the voltage modulation required for switching between full transmission  $T_{on}$  minimal transmission  $T_{off}$ . Minimal transmission occurs at a gate voltage amplitude  $V_G$  that shifts the energy of the incoming WEP with a given  $\beta$ ,  $E_{LP0}(\beta)$  under the gate into the middle of the LP-MP gap [29], which corresponds to:

$$E_{LP0} \simeq E_{hh} - \alpha'(V_G^{off})^2, \quad (S3)$$

and

$$E_{LP0} + \Omega(V_G^{on}) \simeq E_{hh} - \alpha'(V_G^{on})^2, \quad (S4)$$

where  $\alpha' = 1.3/0.85 = 1.53 \text{ meV}/V^2$  is the voltage-dependent polarizability as calculated in Ref. [29]. The transmissive state requires a voltage amplitude modulation that induces an energy shift smaller by  $\Omega(V_G^{on})$ , compared to the blocking voltage,  $V_G^{on} < V_G^{off}$ .

Inverting the equations, the minimal transmission for polariton injected in energy  $E_{LP0}(\beta)$  is given at

$$V_G^{off} = \sqrt{\frac{E_{hh} - E_{LP0}(\beta)}{\alpha'}}. \quad (S5)$$

Maximum transmission is expected at

$$V_G^{on} = \sqrt{\frac{E_{hh0} - (E_{LP0}(\beta) + \Omega(V_G^{on}))}{\alpha'}}. \quad (S6)$$

The voltage modulation is the difference  $V_G^{on} - V_G^{off}$  and is given by:

$$\Delta V_G = V_G^{off} \left( 1 - \sqrt{\frac{E_{hh0} - (E_{LP0}(\beta) + \Omega(V_G^{on}))}{E_{hh0} - E_{LP0}(\beta)}} \right). \quad (S7)$$

We note that the Rabi frequency  $\Omega(V_G)$  decreases with increasing voltage [24], and can be described by  $\Omega(V_G) = \Omega(V_G = 0) \times \exp(-V_G^2/2\sigma_\Omega^2)$ , where  $\sigma_\Omega$  and  $\Omega(V_G = 0)$  are fitting parameter for our system, with values of 11 meV and 4 V, respectively. The experimental data and the model are shown together in Fig. 1(h).

### ENERGY PER OPERATION CALCULATION

To estimate the energy per operation, we consider two scenarios. (1) The device is in an *on*-state all the time. This leads to a constant current (*DC*) of  $I_{on} = 0.46 \mu\text{A}$  at  $V_{on} = -3.1 \text{ V}$ . (2) The device is modulated between the *off* and *on* states with a 50%-50% duty cycle  $f = 1 \text{ GHz}$ . Here the current alternates between  $I_{on}$ ,  $V_{on}$  and  $I_{off} = 0.85 \mu\text{A}$  at  $V_{off} = -0.85 \text{ V}$ . For the *DC* case, the energy per operation is  $U_{DC} = 1.43 \text{ fJ/operation}$ , at the 50%-50% duty cycle, the average current is  $I_{avg} = \frac{I_{on} + I_{off}}{2}$ , and the average voltage is  $V_{avg} = \frac{V_{on} + V_{off}}{2}$ . The energy per operation is then given by  $E_{op,avg} = 1.29 \text{ fJ/operation}$ . The data on which these calculations are based are plotted in Fig.- S1.

The nonlinear response of the system, as reported in Ref. [29], requires  $\sim 5000$  photons for a 500 ps pulse, a 0.5 duty cycle at a 1 GHz repetition rate, to achieve the same DWEP density required for the transistor operation.

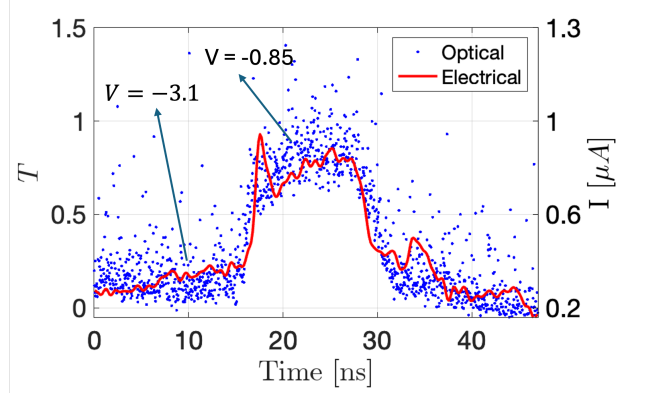


Figure S1. Time-resolved measurement of the electrical current at  $E = -10.5\text{meV}$  (red line) and optical transmission (blue dots) as a function of time. The off voltage is  $V = -3.1\text{V}$  with a ramp of  $\Delta V = 2.25\text{V}$  for transmission. This data was used to calculate the average energy per operation. The optical signal tracks the changes in the system, demonstrating the correlation between electrical and optical properties.

The energy per pulse,  $E_{\text{pulse}}$ , can be calculated as the product of the photon energy ( $E_{\text{ph}}$ ) and the number of photons per pulse ( $N_{\text{ph}}$ ):

$$E_{\text{pulse}} = E_{\text{ph}}N_{\text{ph}}. \quad (\text{S8})$$

For photons with an energy of approximately 1.527 eV, this corresponds to a total of 1.2 fJ per cycle, highlighting the system's remarkable energy efficiency.

### OPTICAL SETUP

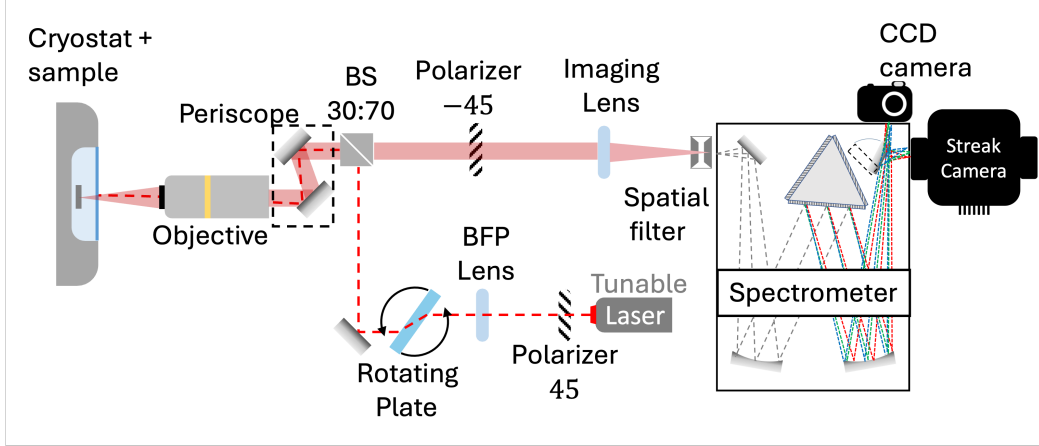


Figure S2. **The optical Setup:** A red dashed line marks the incident light, and a shaded red line marks the emitted light.

The optical setup, presented in Fig. S2, contains a CW Titanium-Sapphire Laser (model 3900 by Spectra-Physics). The laser is focused on the back-focal plane (BFP) of the objective lens, at a spatial location such that it will enter the in-coupling grating at a desired single angle of incidence corresponding to the LP dispersion at a given energy. To choose the angle, we use a glass plate (about 5 mm thick), which deflects the beam to different positions at the BFP, i.e., different angles of incidence. Furthermore, the laser light is polarized at a  $45^\circ$  with respect to the in-coupling grating. The emission path includes cross-polarized light emitted at a  $-45^\circ$  with respect

to the out-coupling grating. This setup is designed to separate the emitted light from the scattered laser light. After the light is emitted from the sample, it is imaged in the entrance slit of a spectrometer. A spatial filter is used to filter out all other emission except from the output grating coupler. The spectrometer has two outputs: a cooled CCD camera and a Streak Camera for imaging or time-resolved experiments respectively.

## ADDITIONAL DATA

Below, we plot the raw data used in the main text and data that supports the measurements in the main text. Figures S3 and S4 shows the Raw-data used for the analysis presented in Figures 1 and 2.

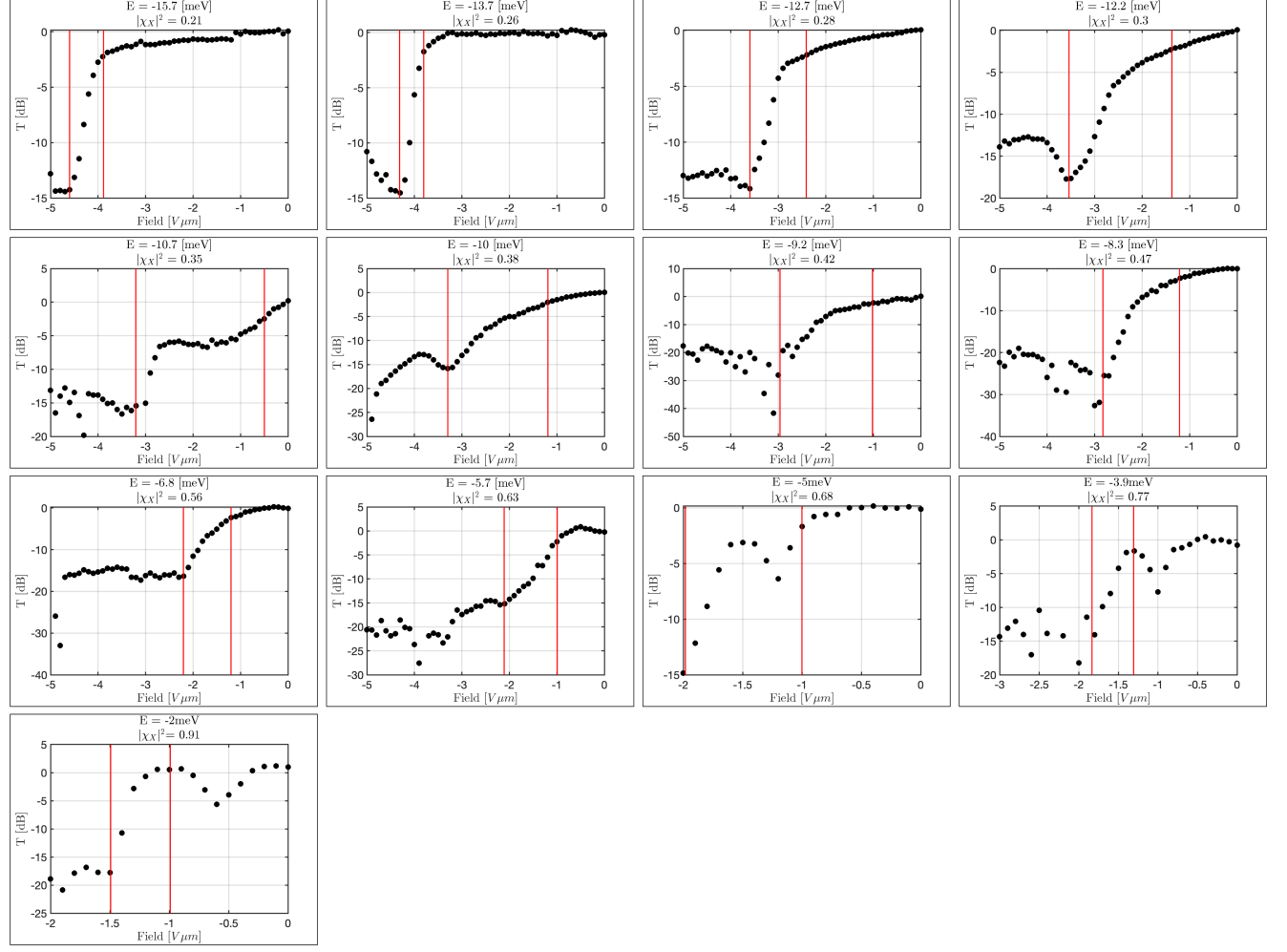


Figure S3. Raw Data of the switching performed with DC electric field, used in Fig. 1(g and h)

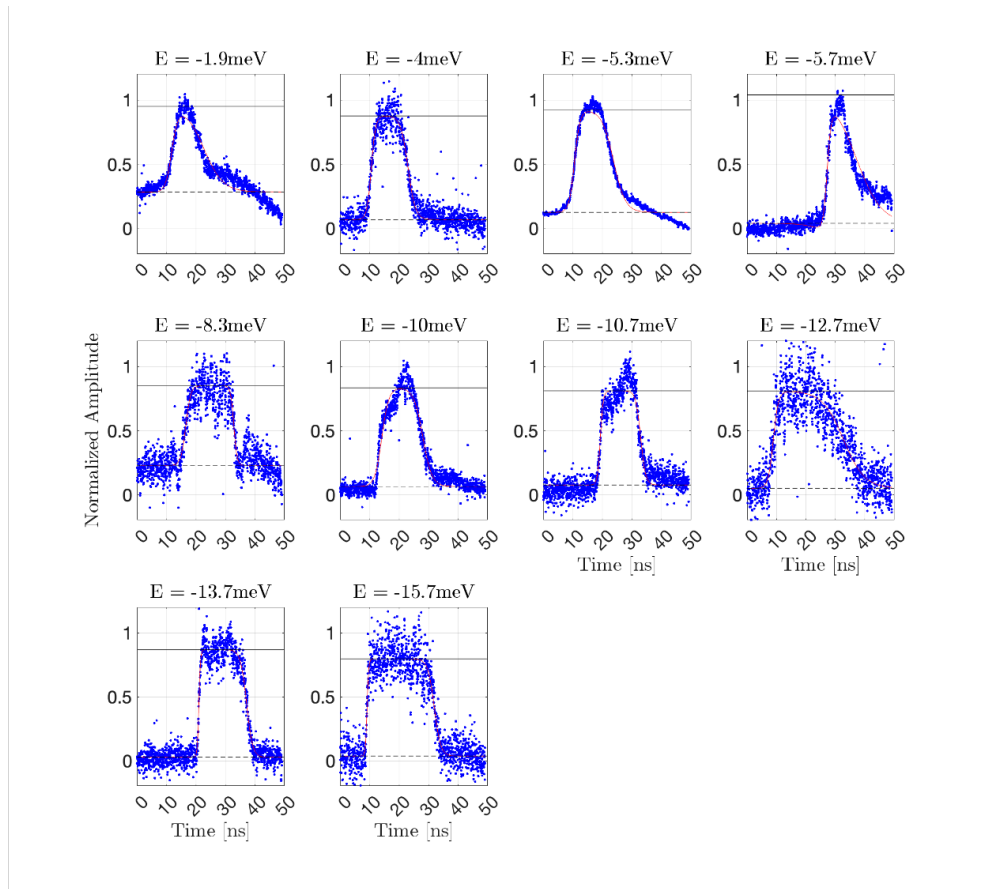


Figure S4. Raw Data of the switching performed with a pulsed electric field, used in Fig. 2(e-f)